Semiautomated Extraction of Street Light Poles From Mobile LiDAR Point-Clouds

Yongtao Yu, Jonathan Li, *Senior Member, IEEE*, Haiyan Guan,
Cheng Wang, *Member, IEEE*, and Jun Yu, *Member, IEEE*

Abstract—This paper proposes a novel algorithm for extracting street light poles from vehicleborne mobile light detection and ranging (LiDAR) point-clouds. First, the algorithm rapidly detects curb-lines and segments a point-cloud into road and nonroad surface points based on trajectory data recorded by the integrated position and orientation system onboard the vehicle. Second, the algorithm accurately extracts street light poles from the segmented nonroad surface points using a novel pairwise 3-D shape context. The proposed algorithm is tested on a set of point-clouds acquired by a RIEGL VMX-450 mobile LiDAR system. The results show that road surfaces are correctly segmented, and street light poles are robustly extracted with a completeness exceeding 99%, a correctness exceeding 97%, and a quality exceeding 96%, thereby demonstrating the efficiency and feasibility of the proposed algorithm to segment road surfaces and extract street light poles from huge volumes of mobile LiDAR point-clouds.

Index Terms—Light pole extraction, mobile light detection and ranging (LiDAR), point-cloud, road surface segmentation, shape context.

I. INTRODUCTION

IN THE past two decades, light detection and ranging (LiDAR) technology has rapidly developed and been used to acquire geospatial information for a variety of applications: urban planning, environmental impact assessment, cultural heritage documentation, intelligent transportation systems, and disaster management. Both airborne LiDAR and vehicleborne mobile LiDAR systems have been widely used for surveying and mapping purposes [1], [2]. From the point-cloud data acquired by the aforementioned systems, algorithms have also been developed for the computerized extraction of buildings [3]–[7], trees [8]–[11], pedestrians [12], [13], roads [14], [15], and digital elevation models [16], [17]. Differing from its airborne counterparts, mobile LiDAR systems have the following advantages: 1) good view of the pavement; 2) direct view of vertical surfaces such as building façades; 3) closer to ground objects; 4) higher point density such as 4000 points/m^2 with a vehicle moving speed of 50 km/h or higher; and 5) visible from

the roadway. Thus, accurately extracting objects from mobile LiDAR point-clouds has attracted more and more attention in remote sensing and mapping communities. As an essential component of the transportation infrastructure, street light poles function to provide vehicles and pedestrians with illumination at night. Cost-effectively monitoring and managing street light poles are important to the transportation management department. Therefore, our interest focuses on the extraction of street light poles from mobile LiDAR point-clouds.

Existing methods for extracting pole-like objects (e.g., light poles) from point-clouds are based on machine learning [18], [19], shape features [20], [21], and prior knowledge [14], [22], [23]. Shape features provide important clues to detect and extract pole-like objects. Such features have been considered and integrated into a principal component analysis (PCA) method in some studies. In [20], based on shape and context features, pole-like objects with tilt angles and various radii were automatically detected using a PCA approach. Shape features of each pole-like object were calculated by height, number of segments, and structure types; however, context features were computed by the surrounding distributions of pole-like objects. Similarly, a covariance-based procedure was presented in [21] to detect road light poles based on eigenvalue analysis. However, instead of analyzing the spatial features of point-clouds in 3-D space, all clustered objects were projected onto a horizontal plane [24]. The distribution of each object was captured by decomposing the covariance matrix of 2-D points into principal components. Objects with linear features (e.g., light poles) were simply detected by comparing the associated eigenvalues.

According to the design and construction manuals for street lighting systems, light poles always have predefined shapes, heights, and sizes that provide essential prior knowledge for the detection and extraction of the light poles. A percentile-based algorithm was introduced in [14] for the recognition of light poles. Instead of analyzing the whole object segment, the segment was first divided into four quartiles [25]. Considering the impact of the shrubs attached at the bottom of a light pole, as well as other attachments to the pole, such as traffic signs and advertising boards, the third quartile was selected and divided into horizontal slices. Finally, light poles were recognized based on the detection of vertical pole-like structures. In [22], a density of projected points (DoPP) algorithm [26], [27] was applied to extract street light poles from point-clouds. First, point-clouds were divided into voxels on the XY plane. Then, the maximum height of each voxel was calculated, and a height threshold, based on the height data, was subsequently determined. Finally, by classifying point-clouds into ground,
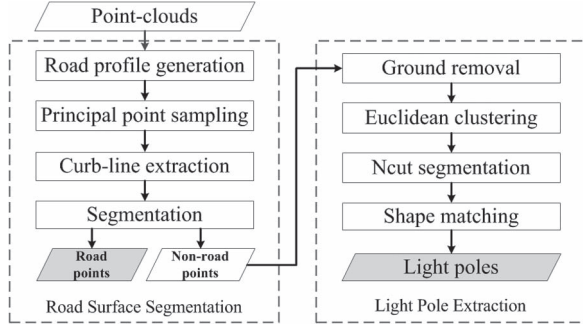
Fig. 1. Flowchart of the proposed algorithm.

low ground, and high ground points, light poles were extracted by simply applying the height threshold.

In general, in order to better capture the surrounding geospatial information, a line scan mode is designed for vehicleborne mobile LiDAR systems. As a result, vertical scan lines were used in [28] to extract utility poles based on the detection of point groups that formed independent vertical scan lines on profiles. Similarly, by using the scan line information on profiles, pole-like objects were extracted by grouping points of each profile and clustering extracted sweeps to form poles [29].

In this paper, we propose a novel algorithm for segmenting road surfaces and extracting street light poles from mobile LiDAR point-clouds. As shown in Fig. 1, the algorithm is carried out based on the following stages: 1) a series of road profiles is generated along the vehicle's trajectory, which is acquired by the integrated global navigation satellite system (GNSS) receiver and inertial measurement unit (IMU); 2) curblines are extracted based on profile analysis and then used to segment the point-clouds into road and nonroad surface points; 3) ground points are further removed from nonroad surface points using a voxel-based elevation filter; 4) the filtered point-clouds are clustered into groups based on a Euclidean distance clustering method; 5) the clusters that contain more than one object are further segmented using a normalized cut segmentation method; and 6) light poles are finally extracted using a novel pairwise 3-D shape context, which is defined for modeling the geometric structure of a 3-D point-cloud object. In summary, the contributions of this paper are as follows: 1) a framework of road surface segmentation based on trajectory and profile analysis; 2) a voxel-based elevation filter for removing ground with strong fluctuations; 3) a voxel-based normalized cut segmentation method for segmenting overlapping objects; and 4) a pairwise 3-D shape context, capable of partial object matching and retrieval, for extracting street light poles.

The remainder of this paper is organized as follows. Section II presents the road surface segmentation method. Section III describes the light pole extraction method. Section IV reports and discusses the experimental results obtained using the RIEGL VMX-450 point-clouds. Finally, Section V gives the concluding remarks.

II. ROAD SURFACE SEGMENTATION

Road surface points can be separated from nonroad surface points based on the following two facts: 1) road locations can be determined by the vehicle's trajectory, and 2) curbs that are
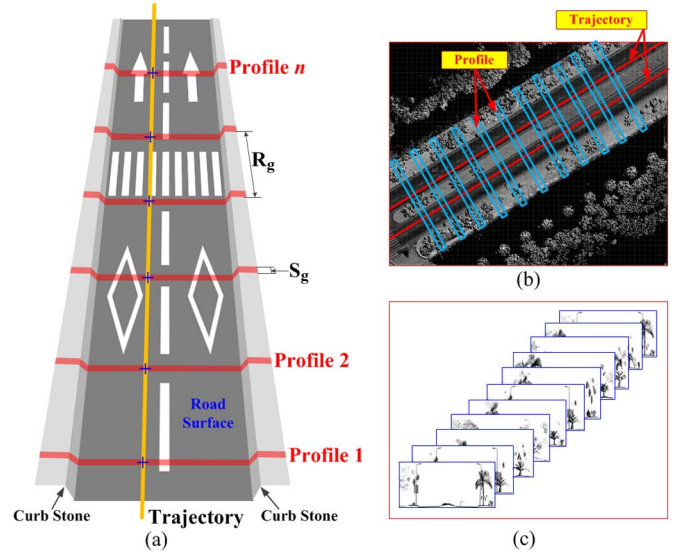

Fig. 2. Point-cloud profiling. (a) Profiling model. (b) Point-cloud with trajectories. (c) Set of profiles shown in (b).

usually located at a height of 10–20 cm above the road surface are designed to separate roads from sidewalks.

A. Profile Generation and Principal Point Sampling

As shown in Fig. 2(a), the raw point-clouds are cross-sectioned into a series of profiles with a certain width (S_g) at a certain distance interval (R_g) perpendicular to the trajectory. Fig. 2(b) shows an example of a raw point-cloud with trajectories; Fig. 2(c) presents a set of profiles. These profiles in Fig. 2(c) show the following: 1) curbs are usually vertical to the road surface, and 2) there is an abrupt increase in curb height. These two properties provide important clues for identifying road boundaries.

Once the profiles have been generated, principal points are sampled from each profile. First, each profile is vertically partitioned into a set of grids with a fixed width (S_p). Second, a principal point is selected from each grid by a layering approach. To this end, all of the points within a grid are first sorted according to their elevations by a quick sort algorithm, followed by a layering criterion. Two consecutive points are grouped into the same layer if and only if their elevation difference lies below a layering threshold (d). The layering criterion is defined as

$$\begin{cases} p_{i-1} \in L_A \wedge p_i \in L_A, & \text{if } z_{p_i} - z_{p_{i-1}} \le d \\ p_{i-1} \in L_A \wedge p_i \in L_B, & \text{otherwise} \end{cases} \quad (1)$$

where L_A and L_B are two different layers, p_{i-1} and p_i are two consecutive points after sorting, and $z_{p_{i-1}}$ and z_{p_i} are their corresponding elevations.

Then, the principal points within each grid are determined by selecting the point with the highest elevation within the lowest layer.

B. Curb-Line Extraction and Road Surface Segmentation

A curb-line can be approximated by a collection of discrete curb corner points detected from the principal points within each profile. In this paper, curb corner points are detected
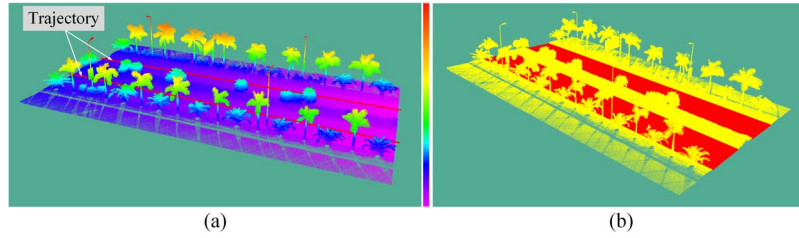
Fig. 3. Road surface segmentation. (a) Raw point-cloud shown in elevation mode. (b) Segmented road surfaces (red).
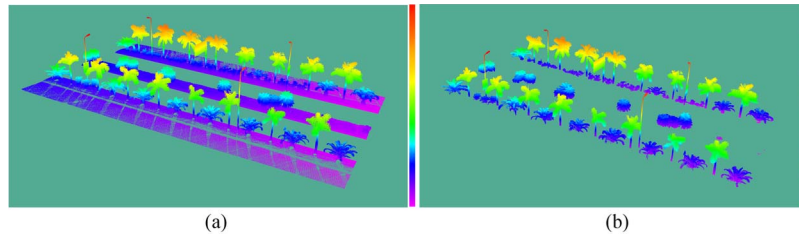

Fig. 4. Point-clouds (a) after road surface segmentation and (b) after ground removal.

based on the following three procedures: 1) elevation gradient computation; 2) elevation gradient filtering; and 3) curb corner point selection.

First, from the point where a profile intersects the trajectory, elevation gradients of the principal points are computed for each profile. The elevation gradient of principal point i is defined as follows:

$$\nabla_i = \begin{cases} z_{p_i} - z_{p_{i-1}}, & \text{point } i \text{ locating on the right side} \\ & \quad \text{of the trajectory} \\ z_{p_i} - z_{p_{i+1}}, & \text{point } i \text{ locating on the left side} \\ & \quad \text{of the trajectory.} \end{cases} \quad (2)$$

Generally, a large elevation gradient indicates a large fluctuation, while a small elevation gradient is possibly caused in the planar region (e.g., road surface). Thus, an abrupt elevation gradient change, centered by the trajectory, is likely to be caused by a curb corner point.

However, objects (e.g., pedestrians and cars) on the road surface, which can also cause abrupt elevation gradient changes, create problems for the detection of curb corner points. Thus, we apply a gradient filter with a low threshold (∇_L) and a high threshold (∇_H) to the principal points to filter out the points with small elevation fluctuations, as well as tall objects on the road surface.

Finally, curb corner points are simply determined by selecting the first two points, nearest to and located on opposite sides of the trajectory, from the remaining principal points. The extracted curb corner points from all profiles are then fitted to form curb-lines using some fitting methods, such as least squares and B-spline. As shown in Fig. 3, based on the knowledge that the point-clouds between two curb-lines belong to the road surface, the point-clouds are easily segmented into road surface and nonroad surface points.

III. LIGHT POLE EXTRACTION

A. Ground Removal

Because of the scan mode of mobile LiDAR systems, the number of points on the ground, including the road surface,

takes up a great portion of the total number of laser points. To reduce spatial and computational complexities, it is helpful to remove the ground points. In Section II, road surface points have already been eliminated; therefore, we need only to further remove the remaining ground points. Considering terrain fluctuations, we propose a novel voxel-based ground removal method.

First, the point-clouds are vertically partitioned into a series of voxels with equal length and width of r_v on the XY plane. Second, within each voxel, the ground points are filtered out by an elevation filter with a threshold of h_v. The voxel-based elevation filter has the following properties: 1) excellent ability to process scenes with strong fluctuations and 2) excellent ability to remove ground points in linear time, i.e., the time complexity of the voxel-based ground removal method is $O(n)$, where n is the total number of data points. Fig. 4 shows the ground removal result, where the colors represent elevation variations.

B. Euclidean Distance Clustering

After removing the ground, off-ground objects are isolated. However, the points belonging to a specific object are discrete and unorganized in the point-cloud. Thus, before extracting light poles, we use some strategies to organize the discrete points into clusters that represent individual objects. In this paper, we introduce a Euclidean distance clustering approach, which clusters points based on their Euclidean distances to their neighbors. Theoretically, an unclustered point is grouped into a specific cluster if and only if its shortest Euclidean distance to the points within this cluster lies below a predefined threshold (d_c). Using the knowledge that light poles always have some geometric constraints, such as height, we eliminate those low-height clusters to reduce computational complexity. Fig. 5 shows the clustering result using the Euclidean distance clustering approach, as well as the filtering result using prior knowledge. In Fig. 5, different colors represent different clusters.

Fig. 5. (a) Clustering result using the Euclidean distance clustering approach. (b) Filtering result using prior knowledge.
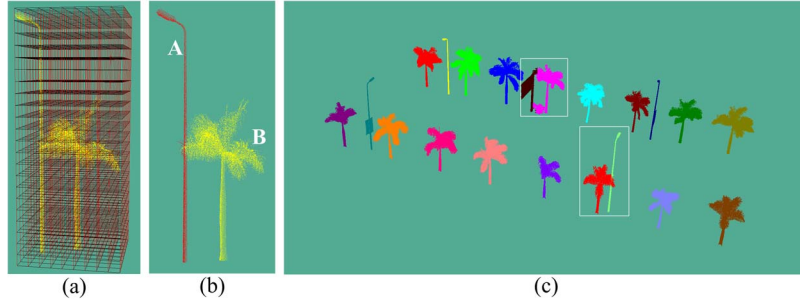

Fig. 6. (a) Voxel partition model. (b) Illustration of bipartition. (c) Ncut segmentation result.

C. Normalized Cut Segmentation

As shown in Fig. 5(b), some clusters contain more than one object (see clusters A and B). Thus, we need to segment these clusters in order to obtain separated objects. To this end, we introduce a normalized cut (Ncut) segmentation method [30], [31]. First, as shown in Fig. 6(a), the cluster is divided into a voxel structure with a voxel spacing of v_e. Second, the nonempty voxels are used to construct a weighted graph $G = \{V, E\}$, where V takes the nonempty voxels as nodes and E is formed between every pair of nodes. The similarity between a pair of nodes $(i, j) \in V^2$ is depicted by the weight w_{ij} which is computed from the features associated with the voxels as follows:

$$w_{ij} = \begin{cases} \exp\left(-\dfrac{\|p_i^{XY} - p_j^{XY}\|_2^2}{\sigma_{XY}^2}\right) \\ \quad \cdot \exp\left(-\dfrac{|p_i^Z - p_j^Z|^2}{\sigma_Z^2}\right), & \text{if } \|p_i^{XY} - p_j^{XY}\|_2 \le d_{XY} \\ 0, & \text{otherwise} \end{cases} \tag{3}$$

where $p_i = (x_i, y_i, z_i)$ and $p_j = (x_j, y_j, z_j)$ are the centroids of voxels i and j, respectively. $p_i^{XY} = (x_i, y_i)$ and $p_j^{XY} = (x_j, y_j)$ are the coordinates of the centroids on the XY plane, and $p_i^Z = z_i$ and $p_j^Z = z_j$ are the z coordinates of the centroids. σ_{XY} and σ_Z are the standard deviations. d_{XY} is a threshold determining the maximal valid horizontal distance between two voxels. The centroid of voxel i is defined as follows:

$$p_i = \frac{1}{N_i} \sum_{m=1}^{N_i} p_m^i \tag{4}$$

where N_i denotes the total number of points within voxel i and $p_m^i (m = 1, 2, \ldots, N_i)$ is a point within voxel i.

As shown in Fig. 6(b), Ncut segmentation aims to partition graph G into two disjoint voxel groups A and B by maximizing the similarity within each voxel group and minimizing the similarity between voxel groups. The corresponding cost function is

$$\text{Ncut}(A, B) = \frac{\text{cut}(A, B)}{\text{assoc}(A, V)} + \frac{\text{cut}(A, B)}{\text{assoc}(B, V)} \tag{5}$$

where $\text{cut}(A, B) = \sum_{u \in A, v \in B} w_{uv}$ is the total sum of weights between voxel groups A and B, and $\text{assoc}(A, V) = \sum_{u \in A, v \in V} w_{uv}$ represents the sum of the weights of all edges ending in voxel group A. The minimization of $\text{Ncut}(A, B)$ is achieved by solving the corresponding generalized eigenvalue problem [30]

$$(\mathbf{D} - \mathbf{W})y = \lambda \mathbf{D} y \tag{6}$$

where $W(i, j) = w_{ij}$ and $\mathbf{D}$ is a diagonal matrix with $D(i, i) = \sum_m w_{im}$.

Finally, by applying a threshold to the eigenvector associated with the second smallest eigenvalue, we partition the cluster into two segments. As shown in Fig. 6(c), the two clusters are correctly segmented into two separated objects, respectively.

D. Construction of Pairwise 3-D Shape Context

Several content-based 3-D shape retrieval methods have been proposed in the literature [32]. Some of these methods use local shape descriptors [33] to model the geometric structure of a shape. However, these descriptors are not affine-invariant. In this section, we define a novel pairwise 3-D shape context (which is affine-invariant and can simultaneously model the local and global geometric structures in manifold space) to model the topology of a 3-D object consisting of a set of discrete points.

Construction of the ROI: Given a clustered object, first, we sample N feature points from the object using the sampling method in [34]. Next, for each pair of feature points (A, B),
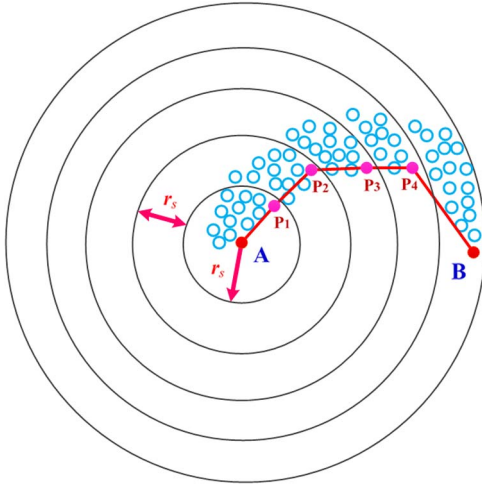
Fig. 7.   Model of computing shortest radial path.

we construct a region of interest (ROI) for describing the point distribution between these two points. To this end, first, we compute a shortest radial path from point A to point B in manifold space. The computation model is shown in Fig. 7. We define a series of concentric spheres $(b_1, b_2, \ldots, b_n)$ with equal radial intervals (r_s) centered at point A. The shortest radial path from point A to point B is defined as

$$P_{AB} = [p_0, p_1, \ldots, p_{n-1}, p_n], \text{ with } A = p_0 \wedge B = p_n \quad (7)$$

where $p_i \in b_i \setminus b_{i-1}(i = 1, 2, \ldots, n-1)$ is the nearest point to p_{i+1}, i.e.,

$$p_i = \arg\min_{p \in b_i \setminus b_{i-1}} \|p - p_{i+1}\|_2, \qquad i = 1, 2, \ldots, n-1. \quad (8)$$

Denote R_{pq} as the direct Euclidean path from point p to point q; then, the shortest radial path P_{AB} is redefined recursively as follows:

$$P_{AB} = \begin{cases} R_{AB}, & B \in b_1 \\ P_{Ap_{n-1}} + R_{p_{n-1}B}, & B \in b_n \setminus b_{n-1} \wedge p_{n-1} \\ & \in b_{n-1} \setminus b_{n-2}. \end{cases} \quad (9)$$

Next, as shown in Fig. 8(a), we create a scalar field as the initial region, within which the points' distances to the shortest radial path P_{AB} are below a threshold r_p. The parameter r_p is the width of the initial region. In practice, in order to adapt the initial region's width to the shortest radial path, we select the width relative to the distance along the shortest radial path and define the width-to-distance ratio as follows:

$$\theta_p = \frac{r_p}{d_{AB}} \quad (10)$$

where d_{AB} is the length of the shortest radial path P_{AB}. Then, we create a filtering region for pruning the initial region. As shown in Fig. 8(b), the filtering region is defined as the intersection of the spherical region centered at point A and the spherical region centered at point B. Finally, as shown in Fig. 8(c), the ROI is constructed by intersecting the initial region and the filtering region.
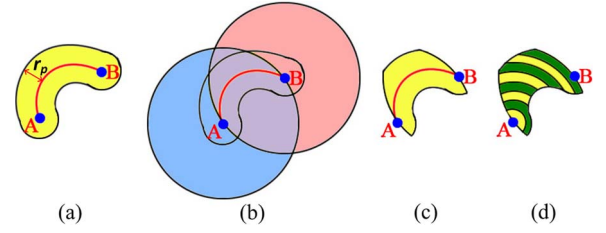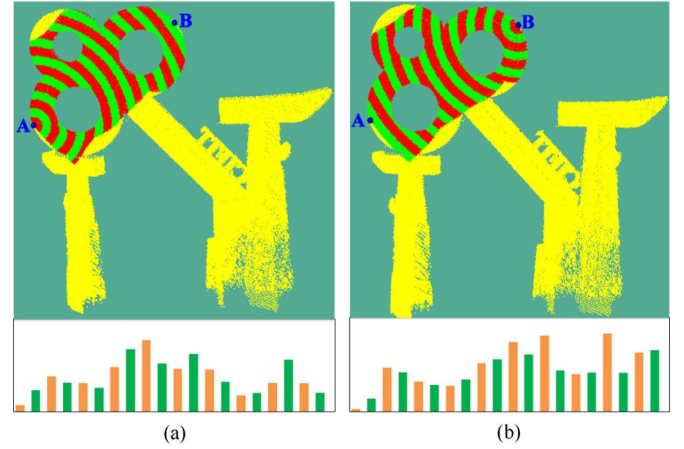

Fig. 8.   ROI construction and bin partition model. (a) Initial region. (b) Filtering region. (c) Constructed ROI. (d) Bin partition model with equal intervals.

Fig. 9.   Directional histogram descriptor. (a) Histogram descriptor for point pair (A, B). (b) Histogram descriptor for point pair (B, A).

Construction of Histogram Descriptors: As shown in Fig. 8(d), once the ROI of the point pair (A, B) has been constructed, we partition the ROI into a set of bins, describing the local statistical distribution between points A and B, with equal radial intervals along the shortest radial path P_{AB}. The interval, denoted by r_b, is determined as follows:

$$r_b = \frac{L_{AB}}{K_b} \quad (11)$$

where L_{AB} is the Euclidean distance between points A and B, and K_b is the bin number. Next, we construct a histogram descriptor by counting the number of points located within each bin and normalizing the number by dividing the total number of points located within the ROI. The histogram descriptor h_{AB} for point pair (A, B) is defined as follows:

$$h_{AB}(k) = \frac{|\text{bin}(k)|}{\sum_{i=1}^{K_b} |\text{bin}(i)|}, \qquad k = 1, 2, \ldots, K_b. \quad (12)$$

Our construction provides a directional histogram descriptor. As shown in Fig. 9, the histogram descriptor h_{AB} for point pair (A, B) is different from the histogram descriptor h_{BA} for point pair (B, A).

Construction of Pairwise 3-D Shape Context: After the histogram descriptors between all pairs of feature points have been constructed, the pairwise 3-D shape context for point p with respect to pairwise combinations with the remaining feature points is constructed as follows:

$$H_p = [h_1^p, h_2^p, \ldots, h_{N-1}^p] \in R^{K_b \times (N-1)}. \quad (13)$$
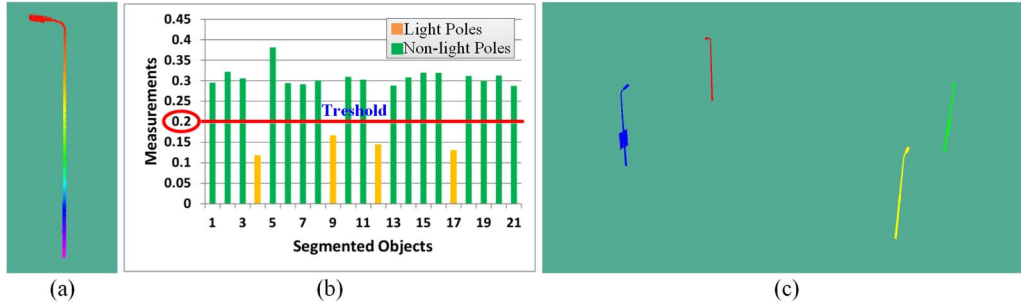
Fig. 10. (a) Light pole prototype. (b) Measurements of clustered objects. (c) Extracted light poles.

E. Light Pole Extraction

In this section, we describe the light pole extraction algorithm in detail. Given a clustered object Q, we use a prototype P [Fig. 10(a)] to identify whether this object is a light pole based on the pairwise 3-D shape contexts of P and Q. The identification criterion is based on the following three factors: one-to-one matching, local dissimilarity, and global dissimilarity.

One-to-One Matching: Consider a point p on prototype P and a point q on object Q. The cost of matching these two points is defined using χ^2 distance as follows:

$$C(p,q) = \min_{i,j=1}^{N-1} \frac{1}{2} \sum_{k=1}^{K_b} \frac{\left[h_i^p(k) - h_j^q(k)\right]^2}{h_i^p(k) + h_j^q(k)}. \quad (14)$$

Then, the cost matrix $C \in R^{N \times N}$, whose entry $C(i,j)$ denotes the cost of matching point i on prototype P and point j on object Q, for matching P and Q is constructed. Finally, the one-to-one matching between the feature points on P and the feature points on Q is given by

$$M_Q(\pi) = \min_\pi \frac{1}{N} \sum_{i=1}^{N} C\left(i, \pi(i)\right) \quad (15)$$

where π is a permutation of $\{1, 2, \ldots, N\}$. This is an instance of the square assignment (or weighted bipartite matching) problem, which can be solved in $O(N^3)$ time using the Hungarian method [35]. In this paper, we use a more efficient algorithm proposed in [36].

Local Dissimilarity: The local dissimilarity between two matched feature points is measured by point curvature. Given a point p, its point curvature is defined using the eigenvalues of the covariance matrix of point p. Thus, we construct a covariance matrix for point p using its k-nearest neighbors $(p_1, p_2, \ldots, p_k)$ as follows:

$$C_p = \frac{1}{k+1} \sum_{i=0}^{k} (p_i - \bar{p}) \cdot (p_i - \bar{p})^T \quad (16)$$

where $p_0 = p$ and $\bar{p} = (1/(k+1)) \sum_{i=0}^{k} p_i$ is the centroid of the $k+1$ points. Next, we decompose the covariance matrix to obtain the eigenvalues λ_0, λ_1, and $\lambda_2 (\lambda_0 \leq \lambda_1 \leq \lambda_2)$, and the associated eigenvectors $\vec{e_0}$, $\vec{e_1}$, and $\vec{e_2}$. Then, the point curvature of point p is computed as follows:

$$\sigma_p = \frac{\lambda_0}{\lambda_0 + \lambda_1 + \lambda_2}. \quad (17)$$

Finally, the local dissimilarity between prototype P and object Q is defined by

$$L(P,Q) = \frac{1}{N} \sum_{i=1}^{N} |\sigma_{p_i} - \sigma_{q_i}|, \; p_i \in P \wedge q_i \in Q. \quad (18)$$

Global Dissimilarity: The global dissimilarity between prototype P and object Q is measured based on the pairwise 3-D shape contexts of P and Q and is defined by the following expression [37]:

$$G(P,Q) = \frac{1}{N(N-1)} \sum_{i=1}^{N} \sum_{j=1}^{N-1} \min_{m,n} \|H_{p_i}(j) - H_{q_m}(n)\|_1. \quad (19)$$

The objective function for identifying object Q is defined as follows:

$$O(Q) = M_Q(\pi) + L(P,Q) + G(P,Q). \quad (20)$$

Finally, based on the objective function, the dissimilarity measurements from all clustered objects are thresholded to extract light poles. Fig. 10(b) shows the measurements of the clustered objects in Fig. 6(c) and the selected threshold for extracting light poles; Fig. 10(c) presents the extracted light poles.

IV. RESULTS AND DISCUSSION

A. Mobile LiDAR Point-Cloud Data Sets

The first mobile LiDAR data were acquired in Xiamen, China. The survey was carried out on Ring Road South, which is a two-directional–four-lane road with a median separating the direction of travel, and covered a total distance of approximately 60 km [Fig. 11(a)]. Due to the data acquisition time and the urban environment, there were many moving cars and pedestrians on the road when collecting the mobile LiDAR data in the daytime. The size of the scanned data, including point-clouds, images, and trajectories, is about 781 GB after postprocessing. The surveyed area, a typical urban area, is located near the seaside and covered with dense vegetation, high buildings, traffic signposts, and light poles on both sides of the road. The light poles are installed every 30 m on both sides of the road. On the average, a 1-km-long point-cloud along the trajectory has a size of about 13 GB but contains only 66 light poles. The
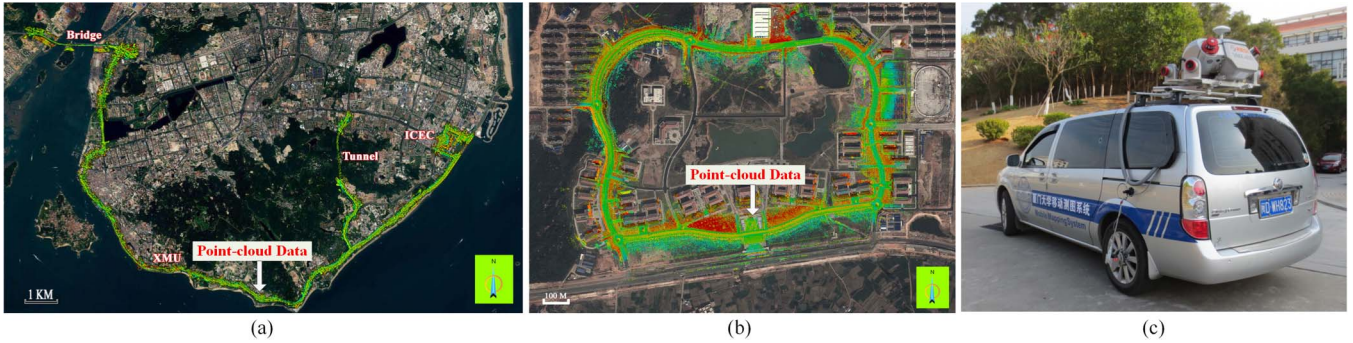
Fig. 11. (a) Xiamen study area and the scanned point-cloud data. (b) Xiangan study area and the scanned point-cloud data. (c) RIEGL VMX-450 system.
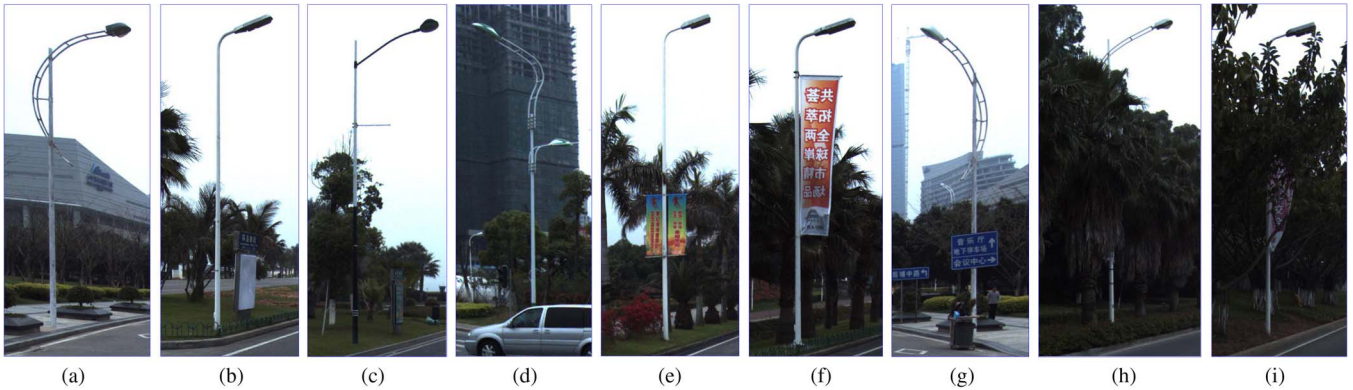

Fig. 12. Illustration of the light poles in the surveyed areas.

second mobile LiDAR data were acquired in Xiangan, China. This survey was carried out on a two-directional–two-lane road in the suburbs and covered a total distance of approximately 34 km [Fig. 11(b)]. This area is a typical suburb with low-height buildings, dense vegetation, and light poles on both sides of the road. There were few moving cars and pedestrians on the road when we collected mobile LiDAR data. The size of the scanned data is about 236 GB after postprocessing. The light poles in this area are installed every 30 m on both sides of the road. For decoration purposes, the light poles are of different shapes and colors [see Fig. 12(a)–(d)]. In addition, some of the light poles have attached traffic signs and advertising boards [Fig. 12(e)–(g)], and some are even hidden in the trees [Fig. 12(h) and (i)]. Therefore, extracting light poles is a great challenge. In our experiments, we selected several data sets containing complex scenes from the scanned data to evaluate our proposed algorithm for extracting light poles.

The mobile LiDAR data were collected by a RIEGL VMX-450 system [Fig. 11(c)], which is smoothly integrated with the following: 1) two full-view RIEGL VQ-450 laser scanners; 2) a GNSS/IMU unit; 3) a wheel-mounted distance measurement indicator; and 4) four high-resolution cameras. The VMX-450 system was mounted on the roof of a caravan moving at an average speed of 50 km/h. The two VQ-450 laser scanners were symmetrically configured on the left and right sides with an "X" pattern. The accuracy of the scanned data is within 8 mm, with a maximum effective measurement rate of 1.1 million measurements per second and a line scan speed of up to 400 scans per second.

B. Parameter Selection for Computing Pairwise 3-D Shape Context

The construction of the pairwise 3-D shape context of an object depends on the following three parameters: the number of feature points (N), the width-to-distance ratio of the ROI (θ_p), and the number of bins (K_b). Hence, the selection of these parameters is essential to the ability of the pairwise 3-D shape context to model the geometric structure of an object. Therefore, we conducted several experiments to test the impacts of different parameter combinations on the extraction of light poles and ascertained the parameter combination with the best performance. As shown in Fig. 13, in our experiments, we selected a set of positive samples containing light poles with different topologies and a set of negative samples containing pole-like objects (nonlight poles) with different topologies.

As shown in Fig. 14, we also calculated the recognition and false recognition rates using different parameter combinations for the positive and negative samples, respectively. After analyzing the test results, in order to balance the recognition and false recognition rates and obtain a good performance in light pole recognition, we selected the parameter combination of $N = 20$, $\theta_p = 0.3$, and $K_b = 30$, which provided a high recognition rate and a low false recognition rate, for the computation of pairwise 3-D shape context in the following experiments.

C. Shape Correspondence

A variety of methods that use shape descriptors for shape correspondence have been proposed in the literature [38]. In this section, we tested the capability of the proposed pairwise
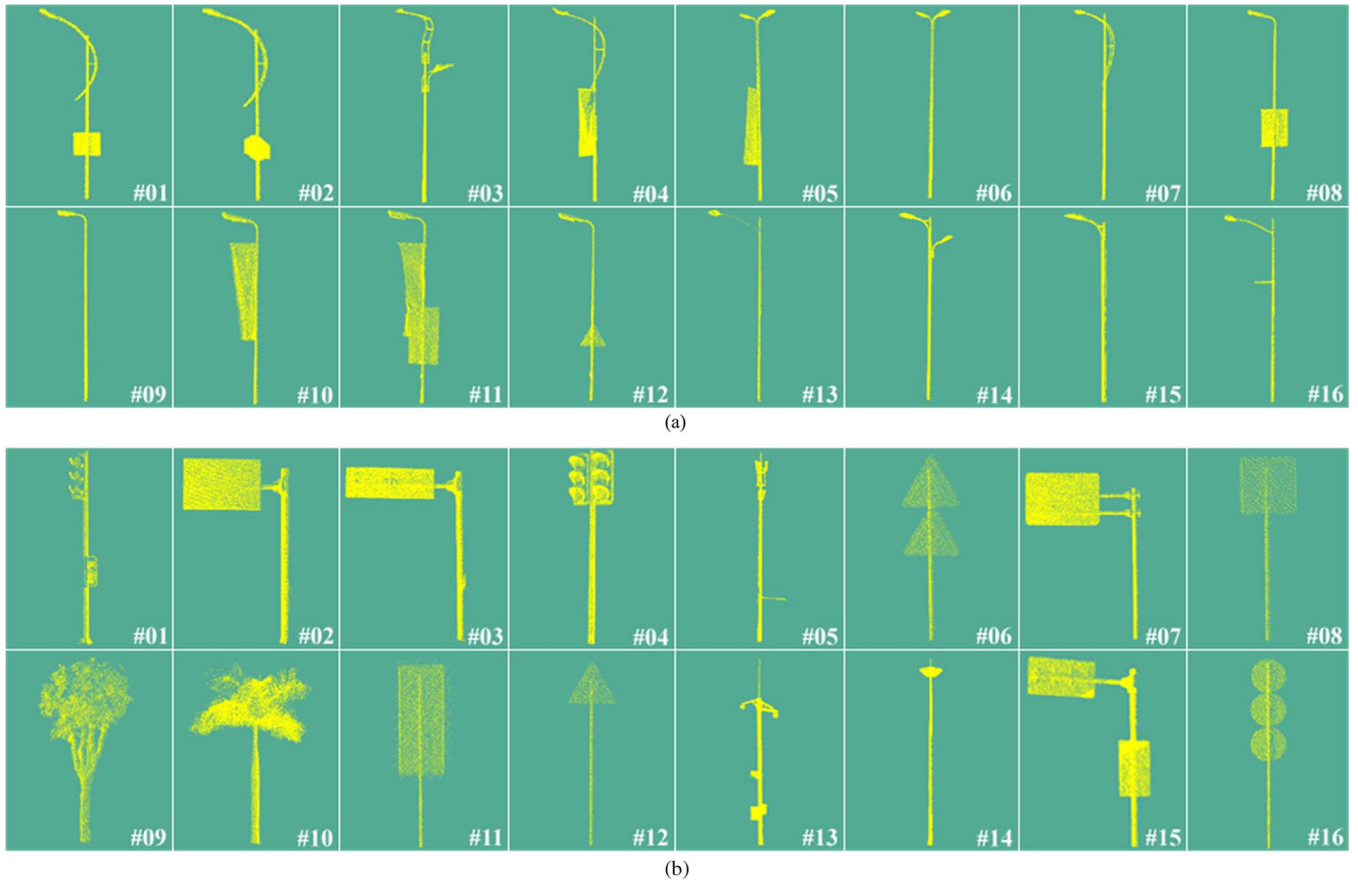
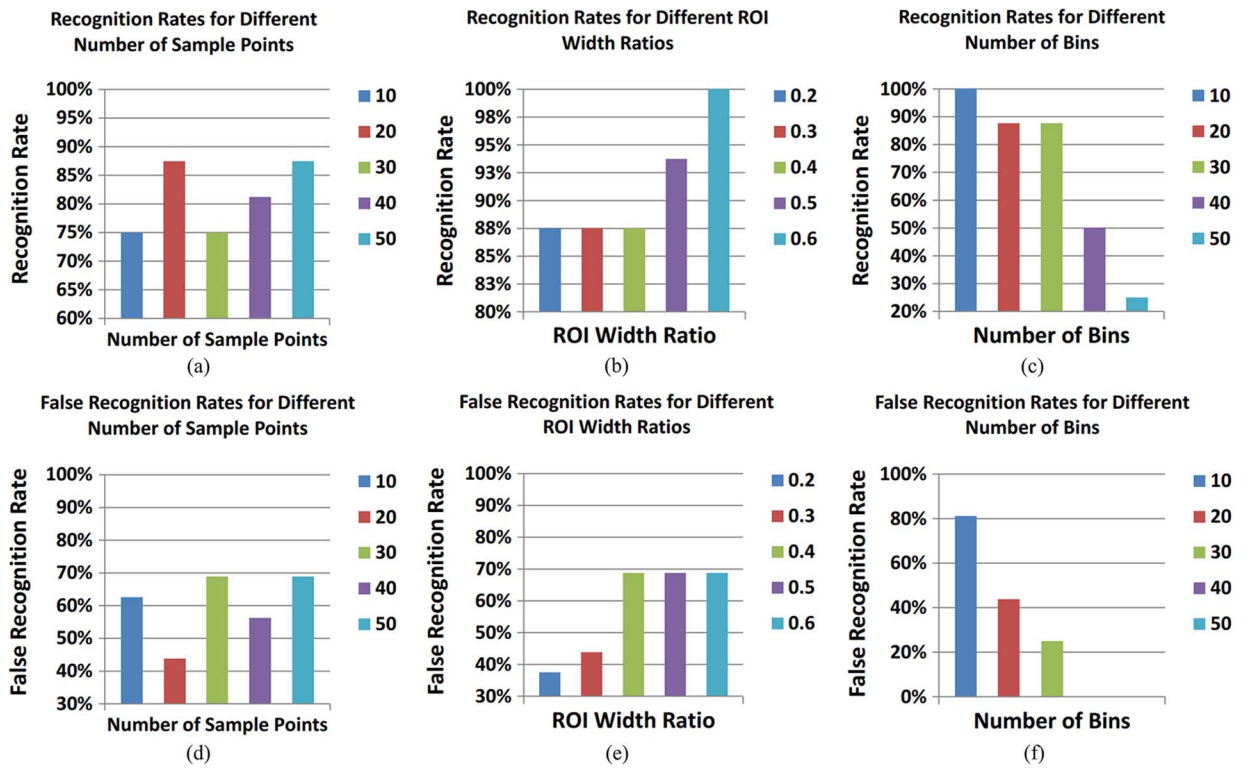Fig. 13.   (a) Positive samples. (b) Negative samples.

Fig. 14.   (a)–(c) Recognition rates for positive samples. (d)–(f) False recognition rates for negative samples. (a) and (d) Testing N with $\theta_p = 0.3$ and $K_b = 20$. (b) and (e) Testing θ_p with $N = 20$ and $K_b = 20$. (c) and (f) Testing K_b with $N = 20$ and $\theta_p = 0.3$.
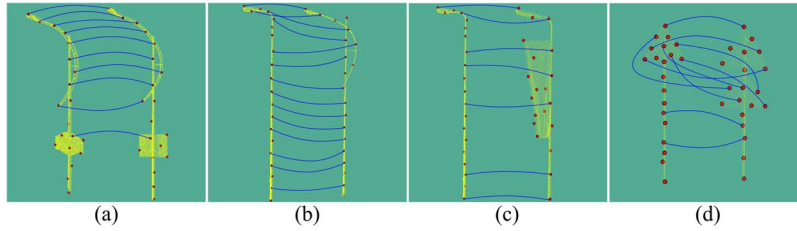
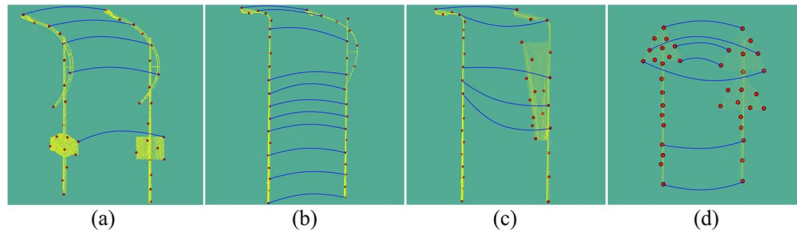Fig. 15. Correspondences computed with the pairwise 3-D shape context.

Fig. 16. Correspondences computed with the single-point 3-D shape context.

TABLE I
DESCRIPTION AND GROUND TRUTH OF THE LIGHT POLE DATA SETS

	Description						Ground Truth		
	Type	Size(GB)	Density(points/m^2)	Lane	Direction	Dim	Clean	Attachment	Total
Dataset-I	Urban	11.12	3873.06	4	2	2	123	118	241
Dataset-II	Urban	16.37	3928.40	4	2	2	103	107	210
Dataset-III	Urban	22.23	4011.35	4	2	2	206	154	360
Dataset-IV	Suburb	16.25	5370.04	2	2	1	289	13	302
Dataset-V	Suburb	19.44	5961.81	2	2	1	299	41	340
Dataset-VI	Suburb	24.31	4932.77	2	2	1	312	76	388

3-D shape context for shape correspondence on point-clouds. Fig. 15 shows visual examples of correspondences computed with the pairwise 3-D shape context. Most of the homologous points are correctly matched between the objects with topological changes. For comparative experiments, we also computed correspondences using the single-point 3-D shape context proposed in [33], as shown by the visual examples in Fig. 16. Comparing the correspondences in Fig. 15 with those in Fig. 16, we conclude that the proposed pairwise 3-D shape context provides more meaningful and correct matches for objects with missing parts or even different topologies and performs better than the single-point 3-D shape context.

D. Light Pole Extraction

In our experiments, we, respectively, selected three data sets, containing street light poles, from the two mobile LiDAR point-clouds acquired in Xiamen and Xiangan. The description of these six data sets is detailed in Table I. The first three data sets were selected from the mobile LiDAR point-cloud acquired in the urban area in Xiamen, and the last three data sets were selected from the mobile LiDAR point-cloud acquired in the suburb in Xiangan. In Table I, "Density" denotes the average point density of the road; "Lane" denotes the number of lanes of the road; "Direction" denotes the number of directions of the road; "Dim" denotes the dimension of the road, where the value of 2 indicates that there is a median on the road for

TABLE II
PARAMETERS USED IN ROAD SURFACE SEGMENTATION

Notation	S_g	R_g	S_p	d	∇_L	∇_H
Value	0.2 m	3.0 m	0.05 m	0.05 m	0.08 m	0.3 m

separating the direction of travel; "Clean" denotes the number of light poles without any attachments, such as traffic signs and advertising boards; "Attachment" denotes the number of light poles with attachments; and "Total" denotes the total number of light poles in the data set. First, we applied the proposed road surface segmentation method to these six data sets to segment road surfaces from the entire point-clouds. The parameters used in road surface segmentation are listed in Table II. Next, light poles are extracted using our proposed algorithm. The parameters used in light pole extraction are listed in Table III. The light pole extraction results of the six data sets are detailed in Table IV. Compared with the ground truth, nearly all light poles, including light poles with and without any attachments, are correctly extracted. Figs. 17 and 18 show parts of the road surface segmentation and light pole extraction results from data set-I and data set-V, respectively. In Fig. 17, a traffic sign (#1) and a palm tree (#2) are falsely detected because of their pole-like features. However, a light pole (#3) that is attached with an advertising board and hidden in a palm tree is well detected by using the Ncut segmentation method. In order to quantitatively evaluate the accuracy of the light pole

TABLE III
PARAMETERS USED IN LIGHT POLE EXTRACTION

Notation	r_v	h_v	d_c	v_e	σ_{XY}	σ_Z	d_{XY}	r_s	θ_p	K_b	N
Value	0.5 m	0.3 m	0.15 m	0.4 m	2.0 m	13.0 m	5.0 m	0.2 m	0.3	30	20

TABLE IV
LIGHT POLE EXTRACTION RESULTS AND ACCURACY EVALUATIONS

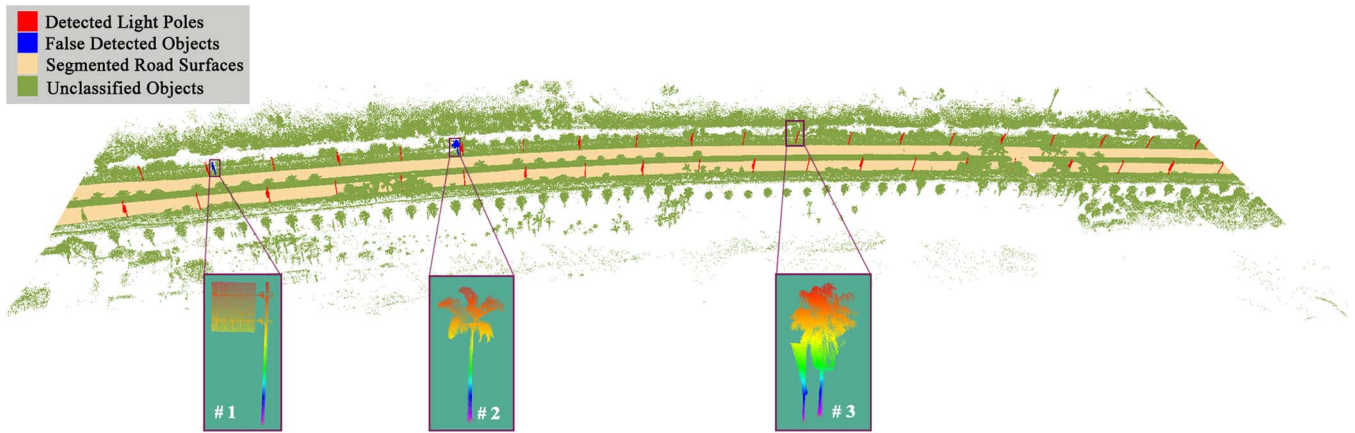|	Extraction Results				Accuracy Evaluations		
	Clean	Attachment	Total	Non-Light Poles	Completeness	Correctness	Quality
Dataset-I	123	116	239	6	99.17%	97.55%	96.76%
Dataset-II	103	105	208	5	99.05%	97.65%	96.74%
Dataset-III	206	153	359	6	99.72%	98.36%	98.09%
Dataset-IV	289	11	300	3	99.34%	99.01%	98.36%
Dataset-V	299	38	337	5	99.12%	98.54%	97.68%
Dataset-VI	312	73	385	4	99.23%	98.97%	98.21%

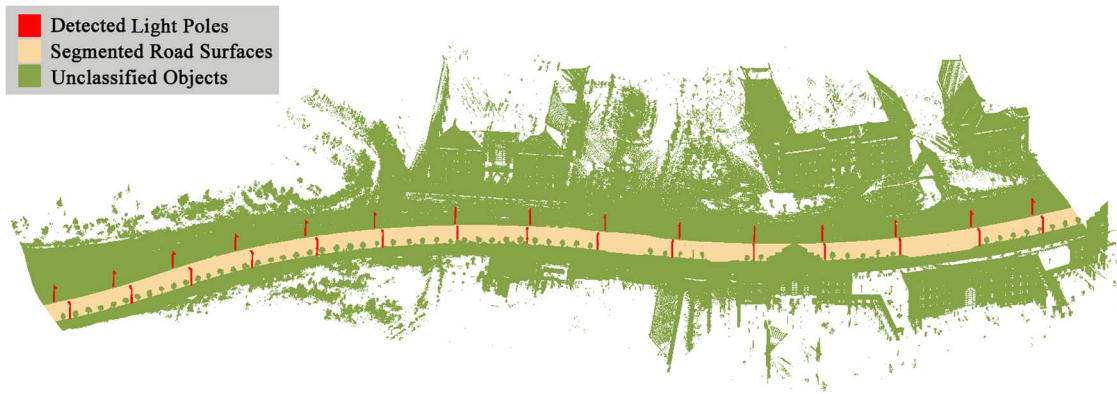Fig. 17. Road surface segmentation and light pole extraction results from data set-I.

Fig. 18. Road surface segmentation and light pole extraction results from data set-V.

extraction results, we introduce three indices [39], including completeness, correctness, and quality. The accuracy evaluation results are listed in Table IV. On the average, the proposed light pole extraction algorithm achieves a completeness greater than 99%, a correctness greater than 97%, and a quality greater than 96%. On the whole, the proposed algorithm segments road surfaces accurately and provides high performance and accuracy in extracting light poles from mobile LiDAR point-clouds.

The proposed algorithm was developed using C++ running on an Intel Core i5 computer. The processing time in each pro-

cessing step and the total processing time for the six data sets are listed in Table V. As seen from Table V, the time complexity of road surface segmentation is quite low. A 6-km-long road (data set-VI) can be segmented within 10.24 s. Moreover, such a big data set with a size of 24.31 GB and containing 388 light poles can be processed within about 51 min. Therefore, the proposed algorithm provides a promising solution to road surface segmentation and street light pole extraction from large-volume mobile LiDAR point-clouds and achieves high performance and accuracy and an acceptable time complexity.

TABLE V
PROCESSING TIME IN EACH PROCESSING STEP

	Processing Time (s)				
	Road Surface Segmentation	Ground Removal	Object Clustering & Segmentation	Light Pole Extraction	Total
Dataset-I	6.40	18.02	429.02	1441.44	1894.88
Dataset-II	5.61	15.75	430.50	1261.26	1713.12
Dataset-III	9.63	27.11	738.14	2162.16	2934.04
Dataset-IV	7.98	21.51	614.05	1701.08	2344.62
Dataset-V	8.96	24.02	688.78	2011.02	2732.78
Dataset-VI	10.24	28.87	787.20	2206.30	3032.61
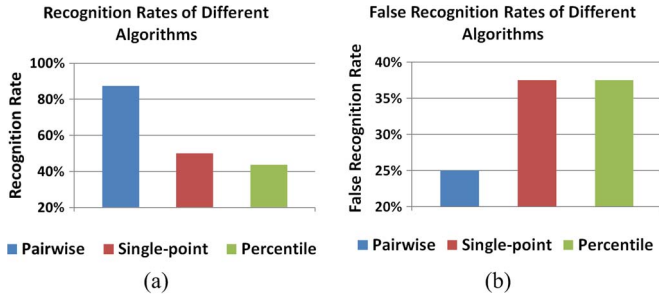
Fig. 19.   (a) Recognition rates of different algorithms. (b) False recognition rates of different algorithms.

Fig. 20.   (a) Raw point-cloud and extracted light poles using (b) our algorithm, (c) the DoPP algorithm, and (d) the PCA-based algorithm.

E. Comparative Studies

In this section, to evaluate the performance of our proposed algorithm, we compared it with other existing algorithms, including the percentile-based algorithm [14], the PCA-based algorithm [21], the DoPP algorithm [22], and the single-point 3-D shape context [33]. First, we compared our algorithm with the single-point 3-D shape context and the percentile-based algorithm. For the single-point 3-D shape context, we replace the pairwise 3-D shape context in (14) and (19) as

$$C(p,q) = \frac{1}{2} \sum_{k=1}^{K_b} \frac{[h_p(k) - h_q(k)]^2}{h_p(k) + h_q(k)} \tag{21}$$

$$G(P,Q) = \frac{1}{N} \sum_{i=1}^{N} \min_j \left\| h_{p_i} - h_{q_j} \right\|_1 \tag{22}$$

where h_i denotes the single-point 3-D shape context of feature point i. Fig. 20 shows the recognition and false recognition rates on the positive and negative samples (see Fig. 13), respectively. As seen from Fig. 19, our algorithm exhibits a higher recognition rate and a lower false recognition rate and performs better than the other two algorithms.

Next, we compared our algorithm with the DoPP and PCA-based algorithms. As seen from the light pole extraction results shown in Fig. 20, our algorithm extracts light poles completely and correctly and obtains better performance than the other two algorithms.

F. Extensive Studies

To further demonstrate the capability of the proposed pairwise 3-D shape context in extracting objects with topological changes, in our experiments, we selected four point-cloud data sets with different types of light poles. We used the same light pole prototype [see Fig. 10(a)] to extract light poles
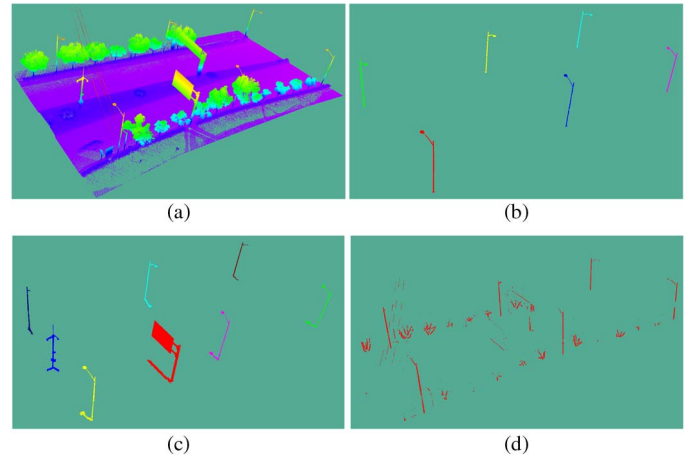
with different shapes from the aforementioned four data sets. The light pole extraction results are presented in Fig. 21. For each of the data sets, light poles are correctly extracted from these point-clouds, regardless of topological changes. Then, we conclude that the proposed pairwise 3-D shape context is capable of matching light poles with topological changes and provides acceptable extraction results.

V. CONCLUSION

In this paper, we have presented a novel algorithm to rapidly segment road surfaces and extract street light poles from large-volume mobile LiDAR point-clouds. The proposed algorithm segments the raw point-clouds into road and nonroad surface points automatically and efficiently. Through profile analysis, curb corner points are detected and then used to guide the segmentation of road surfaces. The algorithm further efficiently and robustly extracts street light poles from the segmented nonroad surface points. Our algorithm contains four steps: 1) ground removal by a voxel-based elevation filter; 2) Euclidean distance clustering for grouping discrete and unorganized points into clusters representing individual objects; 3) normalized cut segmentation for further segmenting clusters containing more than one object; and 4) light pole extraction based on a novel pairwise 3-D shape context. Our proposed algorithm has been evaluated by a set of mobile LiDAR point-clouds in correspondence, road surface segmentation, and light pole extraction. Compared to the single-point 3-D shape context, our proposed pairwise 3-D shape context efficiently
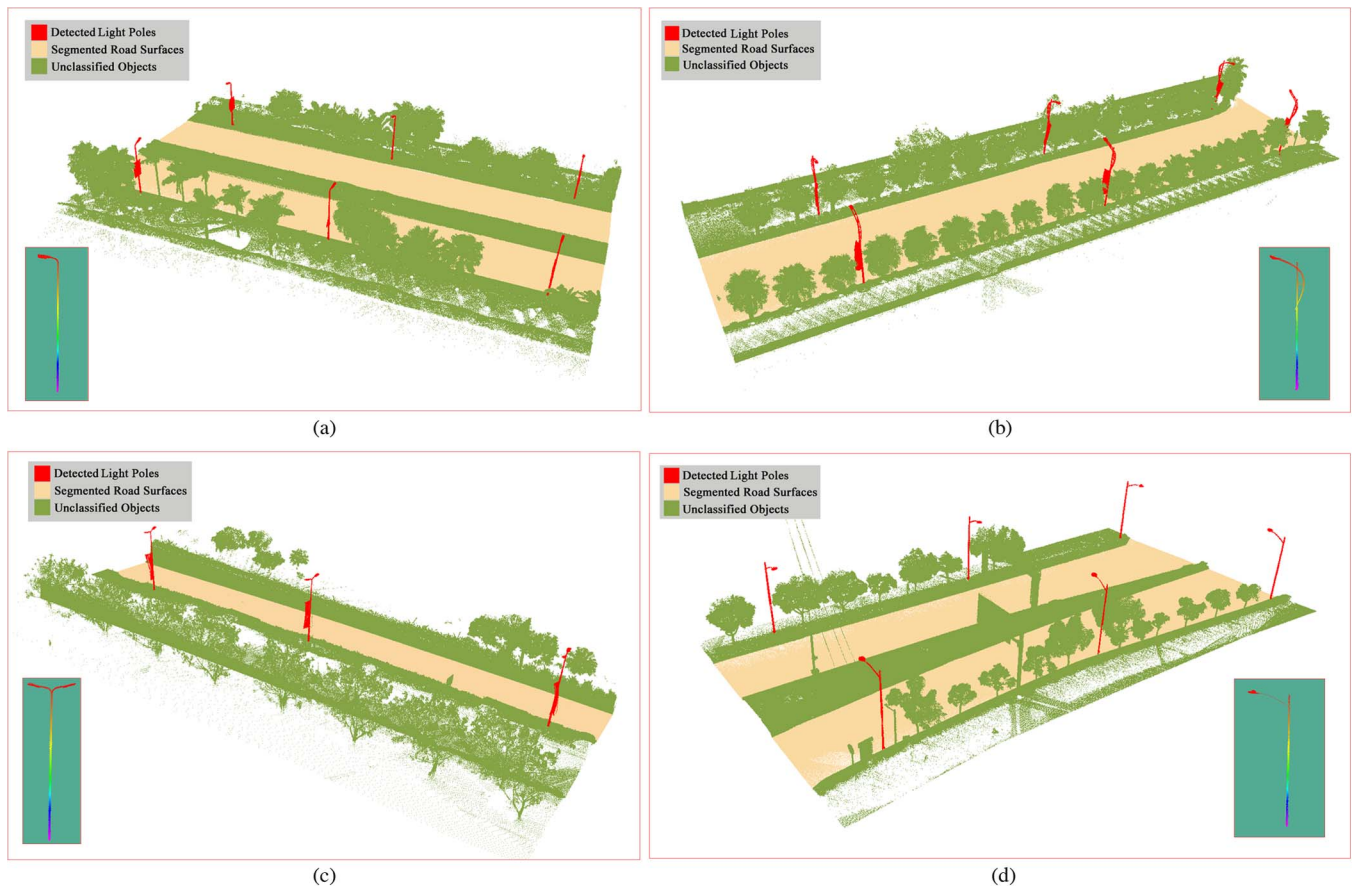
Fig. 21. Extracted light poles with different shapes.

ascertains more meaningful matches and correctly matches more homologous points. Furthermore, compared to the existing light pole extraction methods, our proposed algorithm extracts light poles more correctly and efficiently and achieves a completeness exceeding 99%, a correctness exceeding 97%, and a quality exceeding 96%. Experimental results from a set of mobile LiDAR point-clouds demonstrate the efficiency and feasibility of our proposed algorithm in segmenting road surfaces and extracting street light poles.
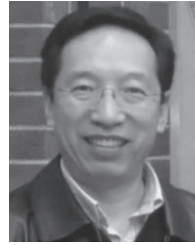
ACKNOWLEDGMENT

REFERENCES

[1] J. Shan and C. Toth, *Topographic Laser Ranging and Scanning: Principles and Processing*. Boca Raton, FL, USA: CRC Press, 2008.

[2] G. Vosselman and H. G. Maas, *Airborne and Terrestrial Laser Scanning*. Boca Raton, FL, USA: CRC Press, 2010.

[3] M. Ortner, X. Descombes, and J. Zerubia, "A marked point process of rectangles and segments for automatic analysis of digital elevation models," *IEEE Trans. Pattern Anal. Mach. Intell.*, vol. 30, no. 1, pp. 105–119, Jan. 2008.

[4] F. Lafarge, X. Descombes, J. Zerubia, and M. Pierrot-Deseilligny, "Automatic building extraction from DEMs using an object approach and application to the 3D-city modeling," *ISPRS J. Photogramm. Remote Sens.*, vol. 63, no. 3, pp. 365–381, May 2008.

[5] R. J. You and B. Lin, "A quality prediction method for building model reconstruction using LiDAR data and topographic maps," *IEEE Trans. Geosci. Remote Sens.*, vol. 49, no. 9, pp. 3471–3480, Sep. 2011.

[6] C. A. Vanegas, D. G. Aliaga, and B. Benes, "Automatic extraction of Manhattan-World building masses from 3D laser range scans," *IEEE Trans. Vis. Comput. Graphics*, vol. 18, no. 10, pp. 1627–1637, Oct. 2012.

[7] B. Yang, Z. Wei, Q. Li, and J. Li, "Semiautomated building façade footprint extraction from mobile LiDAR point clouds," *IEEE Geosci. Remote Sens. Lett.*, vol. 10, no. 4, pp. 766–770, Jul. 2013.

[8] H. Xu, N. Gossett, and B. Chen, "Knowledge and heuristic-based modeling of laser-scanned trees," *ACM Trans. Graph.*, vol. 26, no. 4, pp. 19:1–19:13, Oct. 2007.

[9] Y. Livny *et al.*, "Automatic reconstruction of tree skeletal structures from point clouds," *ACM Trans. Graph.*, vol. 29, no. 6, pp. 151:1–151:8, Dec. 2010.

[10] Y. Livny *et al.*, "Texture-lobes for tree modelling," *ACM Trans. Graph.*, vol. 30, no. 4, pp. 53:1–53:10, Jul. 2011.

[11] Y. Yu, J. Li, H. Guan, C. Wang, and M. Cheng, "A marked point process for automated tree detection from mobile laser scanning point cloud data," in *Proc. Comput. Vis. Remote Sens.*, Xiamen, China, 2012, pp. 140–145.

[12] C. Premebida, G. Monteiro, U. Nunes, and P. Peixoto, "A LiDAR and vision-based approach for pedestrian and vehicle detection and tracking," in *Proc. IEEE Conf. Intell. Transp. Syst.*, Seattle, WA, USA, 2007, pp. 1044–1049.

[13] K. Kidono, T. Naito, and J. Miura, "Reliable pedestrian recognition combining high-definition LiDAR and vision data," in *Proc. IEEE Conf. Intell. Transp. Syst.*, Anchorage, AK, USA, 2012, pp. 1783–1788.

[14] S. Pu, M. Rutzinger, G. Vosselman, and S. O. Elberink, "Recognizing basic structures from mobile laser scanning data for road inventory studies," *ISPRS J. Photogramm. Remote Sens.*, vol. 66, no. 6, pp. S28–S39, Dec. 2011.

[15] B. Yang, L. Fang, and J. Li, "Semi-automated extraction and delineation of 3D roads of street scene from mobile laser scanning point clouds," *ISPRS J. Photogramm. Remote Sens.*, vol. 79, pp. 80–93, May 2013.

[16] C. Wang and N. F. Glenn, "Integrating LiDAR intensity and elevation data for terrain characterization in a forested area," *IEEE Geosci. Remote Sens. Lett.*, vol. 6, no. 3, pp. 463–466, Jul. 2009.

[17] F. Bretar and N. Chehata, "Terrain modeling from LiDAR range data in natural landscapes: A predictive and Bayesian framework," *IEEE Trans. Geosci. Remote Sens.*, vol. 48, no. 3, pp. 1568–1578, Mar. 2010.

[18] A. Golovinskiy, V. G. Kim, and T. Funkhouser, "Shape-based recognition of 3D point clouds in urban environments," in *Proc. IEEE Conf. Comput. Vis.*, Kyoto, Japan, 2009, pp. 2154–2161.

[19] K. Lai and D. Fox, "3D laser scan classification using web data and domain adaptation," in *Proc. Robot.—Sci. Syst.*, 2009, pp. 1–8.

[20] H. Yokoyama, H. Date, S. Kanai, and H. Takeda, "Detection and classification of pole-like objects from mobile laser scanning data of urban environments," *Int. J. CAD/CAM*, vol. 13, no. 2, pp. 31–40, 2013.

[21] S. I. El-Halawany and D. D. Lichti, "Detection of road poles from mobile terrestrial laser scanner point cloud," in *Proc. Int. Workshop M2RSM*, Xiamen, China, 2011, pp. 1–6.

[22] Y. Hu, X. Li, J. Xie, and L. Guo, "A novel approach to extracting street lamps from vehicle-borne laser data," in *Proc. IEEE Conf. Geoinformat.*, Shanghai, China, 2011, pp. 1–6.

[23] M. Lehtomäki, A. Jaakkola, J. Hyyppä, A. Jukko, and J. Kaartinen, "Detection of vertical pole-like objects in a road environment using vehicle-based laser scanning data," *Remote Sens.*, vol. 2, no. 3, pp. 641–664, Feb. 2010.

[24] Y. Chen, H. Zhao, and R. Shibasaki, "A mobile system combining laser scanners and cameras for urban spatial objects extraction," in *Proc. Conf. Mach. Learn. Cybern.*, Hong Kong, 2007, vol. 3, pp. 1729–1733.

[25] D. Luo and Y. Wang, "Rapid extracting pillars by slicing point clouds," in *Proc. ISPRS Congr. IAPRS*, 2008, vol. 37, pp. 215–218.

[26] B. Yang, Z. Wei, Q. Li, and Q. Mao, "A classification-oriented method of feature image generation for vehicle-borne laser scanning point clouds," *Acta Geod. Cartogr. Sin.*, vol. 39, no. 5, pp. 540–545, 2010.

[27] W. Shi, B. Li, and Q. Li, "A method for segmentation of range image captured by vehicle-borne laser scanning based on the density of projected points," *Acta Geod. Cartogr. Sin.*, vol. 34, no. 2, pp. 95–100, 2005.

[28] D. Manandhar and R. Shibasaki, "Feature extraction from range data," in *Proc. the 22nd Asian Conference on Remote Sensing*, Singapore, 2001, vol. 5, pp. 1–6.

[29] A. Kukko, A. Jaakkola, M. Lehtomäki, H. Kaartinen, and Y. Chen, "Mobile mapping system and computing methods for modelling of road environment," in *Proc. Urban Remote Sens. Event*, Shanghai, China, 2009, pp. 1–6.

[30] J. Shi and J. Malik, "Normalized cuts and image segmentation," *IEEE Trans. Pattern Anal. Mach. Intell.*, vol. 22, no. 8, pp. 88–905, Aug. 2000.

[31] J. Reitberger, C. Schnörr, P. Krzystek, and U. Stilla, "3D segmentation of single trees exploiting full waveform LiDAR data," *ISPRS J. Photogramm. Remote Sens.*, vol. 64, no. 6, pp. 561–574, Nov. 2009.

[32] J. W. H. Tangelder and R. C. Veltkamp, "A survey of content based 3D shape retrieval methods," *Multimedia Tools Appl.*, vol. 39, no. 3, pp. 441–471, Sep. 2008.

[33] M. Körtgen, G. J. Park, M. Novotni, and R. Klein, "3D shape matching with 3D shape contexts," in *Proc. 7th Central Eur. Semin. Comput. Graph.*, Budmerice, Slovakia, 2003, vol. 3, pp. 5–17.

[34] D. P. Mitchell, "Spectrally optimal sampling for distribution ray tracing," *ACM SIGGRAPH Comput. Graph.*, vol. 25, no. 4, pp. 157–164, Jul. 1991.

[35] C. Papadimitriou and K. Stieglitz, *Combinatorial Optimization: Algorithms and Complexity*. Englewood Cliffs, NJ, USA: Prentice-Hall, 1982.

[36] R. Jonker and A. Volgenant, "A shortest augmenting path algorithm for dense and sparse linear assignment problems," *Computing*, vol. 38, no. 4, pp. 325–340, Dec. 1987.

[37] O. V. Kaick, H. Zhang, and G. Hamarneh, "Bilateral maps for partial matching," *Comput. Graph. Forum*, vol. 32, no. 6, pp. 189–200, Sep. 2013.

[38] O. V. Kaick, H. Zhang, G. Hamarneh, and D. Cohen-Or, "A survey on shape correspondence," *Comput. Graph. Forum*, vol. 30, no. 6, pp. 1681–1707, Sep. 2011.

[39] M. Rutzinger, F. Rottensteiner, and N. Pfeifer, "A comparison of evaluation techniques for building extraction from airborne laser scanning," *IEEE J. Sel. Topics Appl. Earth Observ. Remote Sens.*, vol. 2, no. 1, pp. 11–20, Mar. 2009.

Jonathan Li (M'00–SM'11) received the Ph.D. degree in geomatics engineering from the University of Cape Town, Cape Town, South Africa, in 2000.

He is currently with the Key Laboratory of Underwater Acoustic Communication and Marine Information Technology (MOE) and the School of Information Science and Engineering, Xiamen University, Xiamen, China. He is also the Head of the Laboratory for GeoSpatial Technology and Remote Sensing, Faculty of Environment, University of Waterloo, Waterloo, ON, Canada, where he is a Professor and an elected member of the University Senate. He is the coauthor of more than 200 publications, over 60 of which were published in refereed journals. His current research interests include information extraction from earth observation images and 3-D surface reconstruction from mobile laser scanning point-clouds.

Dr. Li is the Chair of the Inter-Commission Working Group I/Va on Mobile Scanning and Imaging Systems of the International Society for Photogrammetry and Remote Sensing (2012–2016), the Vice Chair of the Commission on Hydrography of the International Federation of Surveyors (2011–2014), and the Vice Chair of the Commission on Mapping from Remote Sensor Imagery of the International Cartographic Association (2011–2015).

Haiyan Guan received the Ph.D. degree in geomatics from the University of Waterloo, Waterloo, ON, Canada, in 2014.

She is currently a Senior Research Fellow with the Department of Geography and Environmental Management, University of Waterloo. She is the coauthor of more than 30 research papers published in refereed journals, books, and proceedings. Her research interests include airborne, terrestrial, and mobile laser scanning data processing algorithms and 3-D spatial modeling and reconstruction of critical infrastructure and landscape.

Cheng Wang (M'12) received the Ph.D. degree in information communication engineering from the National University of Defense Technology, Changsha, China, in 2002.

He is a Professor and the Vice Dean of the School of Information Science and Engineering, Xiamen University, Xiamen, China. He is the coauthor of more than 80 papers. His current research interests include remote sensing image processing, mobile laser scanning data analysis, and multisensor fusion.

He is the Cochair of ISPRS WG I/3, a council member of the Chinese Society of Image and Graphics, and a member of SPIE and IEEE GRSS.

Yongtao Yu received the B.S. degree in computer science and technology from Xiamen University, Xiamen, China, in 2010, where he is currently working toward the Ph.D. degree in computer science and technology in the Department of Computer Science.

His current research interests include computer vision, machine learning, mobile laser scanning, and information extraction from 3-D point-clouds.

Jun Yu (M'13) received the B.S. and Ph.D. degrees from Zhejiang University, Zhejiang, China.

He is currently a Professor with the School of Computer Science and Technology, Hangzhou Dianzi University, Zhejiang. He was an Associate Professor with the School of Information Science and Technology, Xiamen University, Xiamen, China. From 2009 to 2011, he was with Singapore Nanyang Technological University, Singapore. From 2012–2013, he was a Visiting Researcher with Microsoft Research Asia (MSRA). Over the past years, his research interests include multimedia analysis, machine learning, and image processing. He is the author and coauthor of more than 50 scientific articles.

Dr. Yu is a Professional Member of the ACM and CCF. He was the (co-)chair of several special sessions, invited sessions, and workshops. He served as a program committee member or reviewer of top conferences and prestigious journals.